Hindawi

Research Article

A Proposed Supercapacitor Integrated with an Active Power Filter for Improving the Performance of a Wind Generation System under Nonlinear Unbalanced Loading and Faults

I. Hamdan [ORCID],[1] Marwa M. M. Youssef [ORCID],[1] and Omar Noureldeen [ORCID][1,2]

[1]*Department of Electrical Engineering, Faculty of Engineering South Valley University, Qena 83523, Egypt*
[2]*Department of Electrical Engineering, Faculty of Engineering, Al Baha University, Al Aqiq 65779-7738, Saudi Arabia*

Correspondence should be addressed to I. Hamdan; ibrahimhamdan86@eng.svu.edu.eg

This study proposes the integration of a supercapacitor (SC) with the DC link of a three-phase four-wire active power filter (APF) by using an interfaced three-level bidirectional buck-boost converter controlled by the fuzzy control approach. APF is a flexible alternating current transmission system (FACTS) device that enhances power quality in the electrical network by reducing the load current harmonics and compensating the reactive power. Regulating the DC voltage of the APF's DC link and absorbing fluctuations in compensated reactive power during disturbances are the major objectives of the integration of an SC circuit to APF. The studied model is a wind farm of Gabal El-Zeit with a total capacity of 580 MW, connected to unbalanced nonlinear loads. The Gabal El-Zeit wind farm is divided into three projects with a capacity of 240 MW, 220 MW, and 120 MW. The model is simulated by the MATLAB/SIMULINK program, and the effectiveness of the proposed methodology is proved by applying different types of faults such as single-line-to-ground, double-line-to-ground, and three-line-to-ground faults. In addition, an additional SC circuit with a two-level converter is connected to the generators coupled to the wind turbines to enhance the performance of the wind farm during disturbances. The results show that SC-integrated APF can reduce the harmonic distortion and compensate the reactive power for high or low inductive loads. Also, it can regulate the DC voltage and absorb the fluctuations in the reactive power during faults. Finally, the performance and the stability of the overall electric system are improved.

1. Introduction

The majority of the network's loads are non-linear and unbalanced loads that draw not only active current but also harmonic and reactive current from the AC network, harming the electrical system and other connected devices. Consequently, harmonic suppression and reactive power compensation have gained attention and have been thoroughly researched. Currently, active power filters (APFs) become one of the most efficient tools for controlling harmonics and with a special control, and they can compensate for reactive power consumption. There are many topologies of APF which are shunt APF, series APF, and hybrid APF, as proposed in [1–6]. The shunt APF, which essentially consists of a voltage source inverter (VSI) with a DC link connected to a large capacitor, is said to be a tried-and-true method for bringing the current harmonics down to the advised standard limitations [7]. The study in [8] discusses a novel control of a three-phase half-bridge interleaved buck shunt APF. For a single-phase shunt APF, a fractional-order sliding mode technique method that relies on a double-hidden layer recurrent neural network is suggested in [9]. The research in [10] suggests a new artificial neural network control for APF using the genetic algorithm and employing an optimization technique to adapt the pa-

rameters of the PI control for APF's DC-voltage regulation. Recent studies have focused on the modification of an APF technique; as in [11], the authors designed a universal APF with an adaptive filtering method based on the least mean mixed norm to efficiently extract reactive currents and harmonics. The single-phase shunt APF is proposed in [12] with an enhanced modulated carrier control with on-time double that removes harmonic and reactive currents pulled by nonlinear low frequency. In [13], it is suggested to produce the reference current and control APF using a new deadbeat-based DPC approach. The concept for a shunt APF is suggested in [14] using a single source of power fed to a multilevel inverter with fewer transformers needed. To lower the overall size and cost, a new four-switch two-leg VSI scheme for a three-phase shunt APF is developed in [15]. The current reference control approach for the shunt APF under unbalanced situations is suggested in [16] that uses a combination of the symmetrical component approach and the Kalman filter to determine the fundamental sequence component of the source voltage. The authors in [17] suggest a fault-tolerant control, which combines multicellular topology and two-level topology to boost the dependability of multicellular converters. The study in [18] suggests a predictive power control to reduce fluctuations in DC voltage of the APF using two metaheuristic methods, namely, grey wolf optimizer and ant lion optimizer algorithms. The design of the APF is presented as an optimization problem with many goals, such as enhancing the response time, lowering DC-link voltage overshoot and undershoot, maintaining it at the reference value, and minimizing source current harmonics. The authors in [19] modify a 3-level H-bridge APF with a direct connection to the distribution network. Other recent works of the literature look into ways to enhance APFs by creating new topologies or controller design as in [20]; this study suggests a double-resistive APF which consists of a terminal-resistive APF and an attenuation-resistive APF for each particular harmonic. To prevent harmonic propagation at all harmonic frequencies, the terminal-resistive APF, which acts as the feeder's characteristic impedance, is put at the end bus. To attenuate the appropriate harmonic voltages, the attenuation-resistive APF, whose control gain can be adjusted in accordance with the harmonic voltage distortion limit specifications, is mounted at a precise location for each unique harmonic. The study in [21] investigates how to reduce LCL filter resonance produced by an APF. Novel active damping with a grid-side current component feedback is proposed to address the flaw that typical active damping based on the filter capacitor current or capacitor voltage feedback requires the addition of extra sensors. In [22], a novel high-order passive filter for single-phase half-bridge active power filters is proposed. Parallel resonance is created by paralleling a tiny capacitor with a gird-side inductor, and series resonance is created by adding a small inductor to the capacitor branch loop. In [23], a control technique was proposed to allow the LC-

coupling hybrid APF to function satisfactorily with a small-rating active inverter part for a range of loads. In order to balance active power and compensate for reactive power, the thyristor-controlled LC-coupling component is designed with distinct firing angles for each phase. In [24], the triangular orthogonal principle algorithm serves as the foundation for the new harmonic detection approach presented. The suggested approach has advantages over traditional harmonic current detection methods, such as a simple structure, low calculation requirements, and quick execution times. The shunt APF system is developed in [25] with a fault-tolerant control technique based on improved switch redundancy, and fault tolerance is attained by circuit reconstruction.

As compared to the literature, this research examines how various fault types affect the performance of the APF and suggests a novel method for enhancing performance during fault occurrence by combining the APF with an energy storage system (ESS). This study presents a proposed methodology that suggests using a three-phase four-wire APF integrated with the ESS which is composed of a supercapacitor (SC) and a three-level buck-boost converter controlled by the fuzzy logic control (FLC). This combination technique is named in this study as an SC-integrated APF. The main purposes of the SC circuit are the fluctuation absorption of the compensated reactive power and the regulation of the DC voltage of the APF's capacitor notwithstanding disruptions. The system studied in this study is the wind farm of Gabal El-Zeit with a total capacity of 580 MW. The Gabal El-Zeit wind farm is divided into three projects with a capacity of 240 MW, 220 MW, and 120 MW. There are unbalanced nonlinear loads connected at the point of common coupling (PCC). The wind turbines are driven by the doubly fed induction generator (DFIG) that is composed of a direct grid-connected stator and a rotor connected to the network through a back-to-back converter that is composed of a grid-side converter (GSC) and a rotor-side converter (RSC) with a DC-link capacitor. First, the SC-integrated APF with a low inductive load is studied, and then, a high inductive load is applied. Then, the effectiveness of the system with SC-integrated APF is studied for single-line-to-ground, double-line-to-ground, and three-line-to-ground faults. In addition, this study uses SC with a two-level buck-boost converter at the DC link of the DFIG's back-to-back converter to regulate the DC voltage and improve the performance of the wind farm. This study is organized as follows: The introduction is presented in Section 1. The APF configuration and control are presented in Section 2. The proposed methodology and the studied model configuration are illustrated in Section 3 and Section 4, respectively. Section 5 presents the simulated results and discussion. Lastly, Section 6 displays the findings.

2. Shunt Active Power Filters

Shunt APFs inject an equal but opposing harmonic compensatory current to reduce current harmonics. At the same time, the APF can take on the function of the STATCOM,

which is compensating the reactive power, and this is done through a special control instead of using an additional flexible alternating current transmission system (FACTS) devices. The cost of new elements may be significantly lowered in this method. One of the various objectives of the APF controllers is the decrease in neutral current for unbalanced nonlinear loads. Shunt APFs are normally implemented with a VSI that works as a current-controlled voltage source. Such technologies are often implemented using two-level PWM-VSIs that are coupled through a transformer to the AC system. Figure 1 displays the APF's configuration components which are the VSI, DC-link capacitor, and filtering inductor used to decrease the harmonic currents that circulate as a result of inverter switching and control units.

The control configuration scheme of the APF is illustrated in Figure 2. The main parts of the control are calculation of the compensated currents, current reference generator, DC voltage control, and current control [26].

To create reference currents, the principle of instantaneous reactive power is used. This theory uses equations (1) and (2) to convert the instantaneous load current (i_a, i_b, and i_c) and phase voltage (v_a, v_b, and v_c) to $\alpha\beta$ coordinate components of voltages (v_α, v_β) and currents (i_α, i_β) [26]:

$$\begin{bmatrix} i_\alpha \\ i_\beta \end{bmatrix} = \sqrt{\frac{2}{3}} \begin{bmatrix} 1 & \dfrac{-1}{2} & -\dfrac{1}{2} \\ 0 & \dfrac{\sqrt{3}}{2} & -\dfrac{\sqrt{3}}{2} \end{bmatrix} \cdot \begin{bmatrix} i_a \\ i_b \\ i_c \end{bmatrix}, \tag{1}$$

$$\begin{bmatrix} v_\alpha \\ v_\beta \end{bmatrix} = \sqrt{\frac{2}{3}} \begin{bmatrix} 1 & \dfrac{-1}{2} & -\dfrac{1}{2} \\ 0 & \dfrac{\sqrt{3}}{2} & -\dfrac{\sqrt{3}}{2} \end{bmatrix} \cdot \begin{bmatrix} v_a \\ v_b \\ v_c \end{bmatrix}. \tag{2}$$

Using equations (3) and (4), current and voltage are used in the $\alpha\beta$-coordinate to compute time-dependent active and reactive power (p, q):

$$p(t) = v_\alpha(t).i_\alpha(t) + v_\beta(t).i_\beta(t), \tag{3}$$

$$q(t) = -v_\alpha(t).i_\beta(t) + v_\beta(t).i_\alpha(t). \tag{4}$$

A new instantaneous space vector is provided by vector equation (5) in order to calculate the immediate reactive power:

$$q = v_\alpha \times i_\beta + v_\beta \times i_\alpha, \tag{5}$$

where q is a vector perpendicular to the α, β coordinates plane; the following equation provides the formula for the currents in the plane in terms of the instantaneous power:

$$\begin{bmatrix} i_\alpha \\ i_\beta \end{bmatrix} = \frac{1}{v_\alpha^2 + v_\beta^2} \cdot \left\{ \begin{bmatrix} v_\alpha & v_\beta \\ v_\beta & -v_\alpha \end{bmatrix} \cdot \begin{bmatrix} p \\ 0 \end{bmatrix} + \begin{bmatrix} v_\alpha & v_\beta \\ v_\beta & -v_\alpha \end{bmatrix} \cdot \begin{bmatrix} 0 \\ q \end{bmatrix} \right\} = \begin{bmatrix} i_{\alpha p} \\ i_{\beta p} \end{bmatrix} + \begin{bmatrix} i_{\alpha q} \\ i_{\beta q} \end{bmatrix}, \tag{6}$$

where $i_{\alpha p}$, $i_{\alpha q}$, $i_{\beta p}$, and $i_{\beta q}$ are the different components of the currents in the α, β plane relating to active and reactive power. Each of the instantaneous power p and q is expressed as a summation of the DC component ($\overline{p}$, $\overline{q}$) and the AC component ($\widetilde{p}$, $\widetilde{q}$) as expressed in the following equations:

$$p = \overline{p} + \widetilde{p}, \tag{7}$$

$$q = \overline{q} + \widetilde{q}, \tag{8}$$

where $\overline{p}$ and $\overline{q}$ are concerned with the fundamental active and reactive component of current, respectively, $\widetilde{p}$ and $\widetilde{q}$ are concerned with the harmonic currents produced by the active and reactive instantaneous power's AC component. Equations (9) and (10) are used to determine the compensating reference currents in the $\alpha\beta$-reference frame ($i_{c\alpha}^*$, $i_{c\beta}^*$) and a, b, c reference frame (i_{ca}^*, i_{cb}^*, i_{cc}^*), respectively [26]:

$$\begin{bmatrix} i_{c,\alpha}^* \\ i_{c,\beta}^* \end{bmatrix} = \frac{1}{v_\alpha^2 + v_\beta^2} \cdot \begin{bmatrix} v_\alpha & v_\beta \\ v_\beta & -v_\alpha \end{bmatrix} \cdot \begin{bmatrix} \widetilde{p}_L \\ \overline{q}_L + \widetilde{q}_L \end{bmatrix}, \tag{9}$$

$$\begin{bmatrix} i_{c,a}^* \\ i_{c,b}^* \\ i_{c,c}^* \end{bmatrix} = \sqrt{\frac{2}{3}} \cdot \begin{bmatrix} \dfrac{1}{\sqrt{2}} & 1 & 0 \\ \dfrac{1}{\sqrt{2}} & -\dfrac{1}{2} & \dfrac{\sqrt{3}}{2} \\ \dfrac{1}{\sqrt{2}} & -\dfrac{1}{2} & -\dfrac{\sqrt{3}}{2} \end{bmatrix} \cdot \begin{bmatrix} -i_0 \\ i_{c,\alpha}^* \\ i_{c,\beta}^* \end{bmatrix}. \tag{10}$$

The hysteresis current control receives these reference currents in order to produce switching pulses. To reduce voltage fluctuations without increasing the DC capacitor's capacitance, a control unit for the DC voltage of the capacitor is necessary. The DC-voltage control unit is responsible for maintaining the DC voltage constant which is
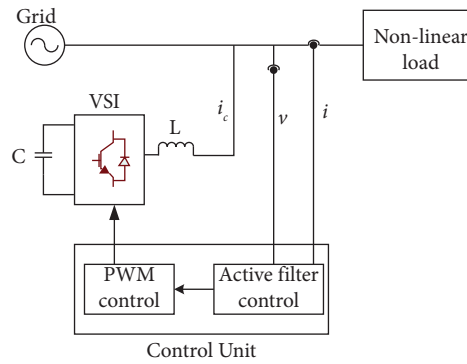
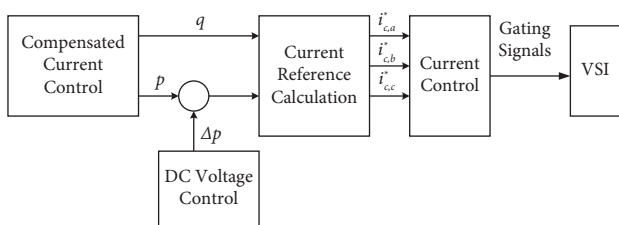FIGURE 1: Configuration components of the APF.

FIGURE 2: The control configuration scheme of the APF.

necessary for tracking compensation requirements. This control generates Δp which indicates the active power that is transferred between the compensator and the source, and this value is necessary for the DC voltage of the capacitor to be maintained at or close to the predetermined normal value. As a result, to make the APF comfortably run, the DC voltage at the DC capacitor needs to be strictly managed. Figure 3 shows another topology that uses a three-phase four-wire APF with a DC capacitor split into two-identical capacitors ($C1$ and $C2$) [27]. The voltages on these capacitors are equal and represented by v_1 and v_2. This arrangement aids in minimizing the neutral current.

3. Proposed Methodology

The proposed methodology suggests the integration of SC with the DC link of APFs by using an interfaced three-level bidirectional buck-boost converter. The main objectives of the SC circuit are to keep the DC voltage of two-split capacitors constant under disturbances and absorb fluctuations in the compensated reactive power. The control technique used with the proposed methodology in this study is the fuzzy control approach. The topology configuration of the SC-integrated APF system employed in this work is shown in Figure 4.

3.1. Principle of Operation for the Three-Level Bidirectional DC-DC Converter with an SC Module. An interfaced three-level buck-boost converter is required to couple the SC circuit to the APF to maintain the DC voltage of the APF's capacitor at the predetermined value. The configuration of the three-level converter is illustrated in Figure 5. It consists of four IGBTs ($Q1$, $Q2$, $Q3$, and $Q4$) and an inductor (L). Two
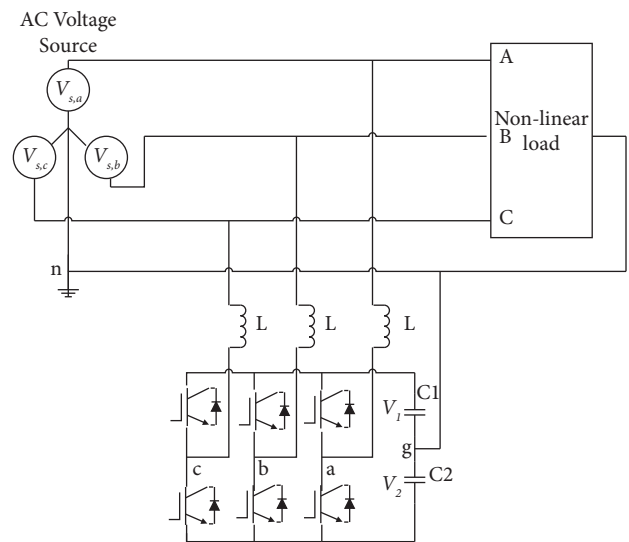

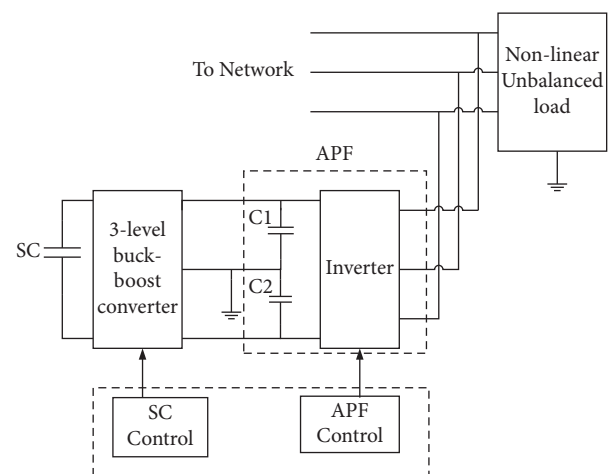FIGURE 3: The arrangement of the three-phase four-wire APF.

FIGURE 4: The topology configuration of the SC-integrated APF system.

triangular waves with a 180° phase shift are used as the carrier signals for switches $Q2$ and $Q3$. ($Q1$, $Q2$) and ($Q3$, $Q4$) are complementary IGBT switch pairs.

It appears that there are four charging states: In state 1, $C2$ is charging when $Q2$ is on and $Q3$ is off. In state 2, $C1$ is charging when $Q2$ is off and $Q3$ is on. In state 3, $C1$ and $C2$ are charging when $Q2$ and $Q3$ are both off. In state 4, $C1$ and $C2$ are not affected, that is, when $Q2$ and $Q3$ are both on. It is possible to write the instantaneous output voltage between a and b (V_{ab}) as follows:

$$V_{ab} = (1 - Sf_2) V_1 + (1 - Sf_3) V_2, \tag{11}$$

where Sf_2 and Sf_3 are the switching functions of switches $Q2$ and $Q3$ and V_1 and V_2 are the voltages on $C1$ and $C2$. It is clear from the diagram that V_{ab} is suited for displaying the capacitor that is now charging, which illustrates how this converter works. In a carrier period at a steady state, i_L (current through the inductor) increases and declines equally. Therefore, according to the volt-second balancing principle, input and output voltages are connected to duty cycles D_{q2} and D_{q3} as follows:

$$\frac{V_{sc} - V_1}{L} D_{q3} T + \frac{V_{sc} - V_2}{L} D_{q2} T = \left(1 - D_{q2} - D_{q3}\right) \frac{V_1 + V_2 - V_{sc}}{L} T, \tag{12}$$

where V_{sc} is the SC voltage, D_{q2} and D_{q3} are the duty cycles of $Q2$ and $Q3$, T stands for the carrier period, and L is the inductance value of the inductor. Since D_{q2} and D_{q3} are equivalent to D and V_1 and V_2 are equivalent to V, equation (12) can be written as follows:

$$V_{out} = 2V = \frac{V_{sc}}{1 - D}. \tag{13}$$

The following equation explains what the step-up ratio (K) is

$$K = \frac{V_1 + V_2}{V_{sc}}. \tag{14}$$

The zone of K identifies three scenarios: when $K = 1$, $Q2$ and $Q3$ are turned off, the SC charges $C1$ and $C2$ automatically until $V_1 + V_2 = V_{sc}$. Figure 6(a) illustrates the scenario when $1 < K < 2$, V_1, $V_2 < V_{sc}$, and i_L rises, charging the output like a buck circuit, this occurs in paths (1) and (3). In path (2), where $V_1 + V_2 > V_{sc}$, i_L decreases, and it operates as a buck circuit to each capacitor. Figure 6(b) illustrates the scenario when $K > 2$, V_1, $V_2 > V_{sc}$, and i_L drops, charging the output like a boost circuit, this occurs in paths (1) and (3). In path (2), where $V_{ab} = 0$, similar to the boost circuit charging the inductance procedure, i_L rises. It equals a boost circuit for each capacitor as a consequence.

3.2. Control Methodology. The following main goals that the SC-integrated APF serves are the basis for developing the control mechanism:

(1) To maintain the DC voltage constant during disturbance

(2) To absorb reactive power fluctuations during faults and disturbance

In this study, the fuzzy control is applied for balancing the DC voltage instead of using conventional control methods. The fuzzy control can deal with the complexity and uncertainty of the system. Figure 7 illustrates the closed-loop control of the SC circuit.

The voltage at the DC link of the APF is measured and compared with its reference value to calculate the voltage error. The error and its differential value are the inputs to the fuzzy control which determines the required value of the change in the duty cycle. The pulse generator generates the signal required to control the IGBT switches of the three-level converter connected to the SC. The membership functions of the fuzzy inputs and outputs are shown in Figure 8, where the fuzzy sets of the inputs are positive (P), zero (Z), and negative (N). The fuzzy sets of the change in the duty cycle are positive big (PB), positive (P), zero (Z), negative (N), and negative big (NB). The fuzzy rules are illustrated in Table 1 that shows the ninth linguistic fuzzy rules which have been used in the fuzzy control structure using "IF-Then" format.

3.3. Additional SC Circuit Connection. In order to improve the system as a whole, this study suggests adding an additional ESS to the back-to-back converter of the DFIG driven by wind turbines. The applied ESS is composed of SC with a two-level buck-boost converter, as shown in Figure 9.

By charging and discharging SC through the buck-boost converter, the DC-link voltage remains constant during disturbances. As a result, the performance and stability of the wind farm are improved. The control of the two-level buck-boost converter using the fuzzy control is shown in Figure 10.

4. Studied Model Configuration

The studied model configuration in this study is a large-scale wind farm of Gabal El-Zeit, as illustrated in Figure 11. The station is located in the area of the Red Sea Governorate in Egypt. The total capacity of the station is about 580 MW, with 300 wind turbines divided into 3 projects. There are 120 turbines in the first project, which has a 240 MW maximum output. The second project includes 110 turbines, with a total capacity of 220 MW. The last project includes 60 turbines which has a 120 MW capacity [28–30]. The model is simulated using MATLAB/SIMULINK by three separated wind turbine blocks that present the three projects, each scaled by 20 MW, so the projects are simulated as 240 MW (12 MW × 20), 220 MW (11 MW × 20), and 120 MW (6 MW × 20). The wind turbines in this model are driven by DFIGs. The wind farm is connected to the grid through transformers and transmission lines. The nonlinear
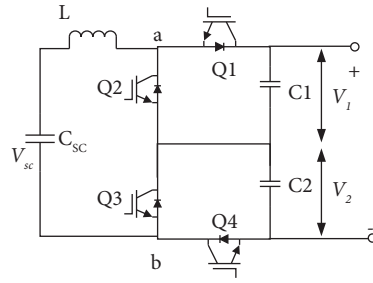
FIGURE 5: The configuration of the three-level buck-boost converter.
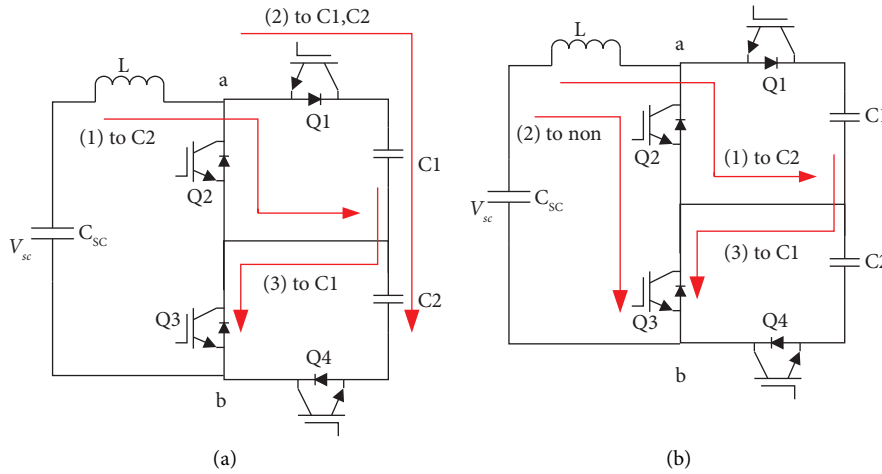

(a)   (b)

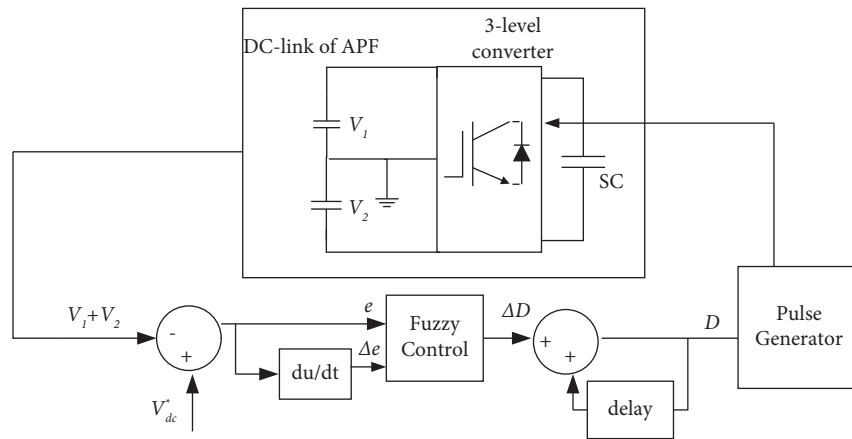FIGURE 6: Charging state of the three-level buck-boost converter. (a) $1 < k < 2$; (b) $k > 2$.
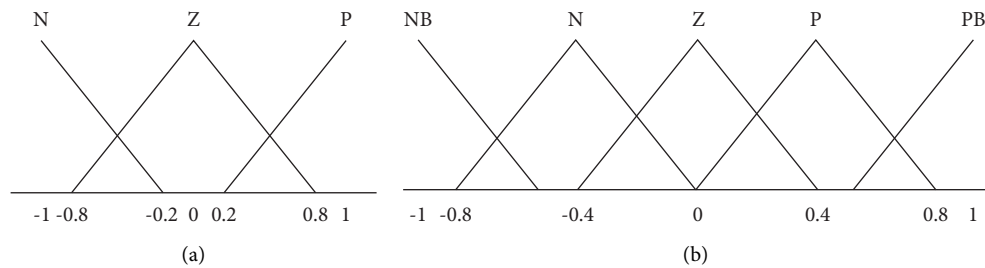

FIGURE 7: Closed loop control of the SC circuit.

(a)   (b)

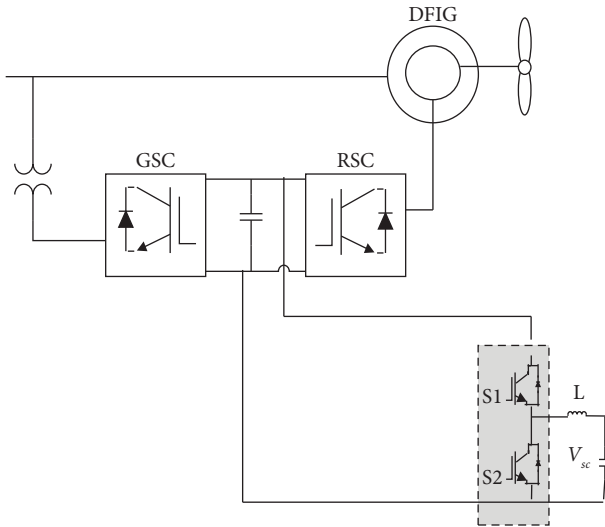FIGURE 8: The fuzzy sets of (a) inputs and (b) output.

TABLE 1: Fuzzy rule base.

Δe	e		
	N	Z	P
N	NB	N	Z
Z	N	Z	P
P	Z	P	PB

FIGURE 9: Connection of SC with a two-level buck-boost converter to the DFIG.
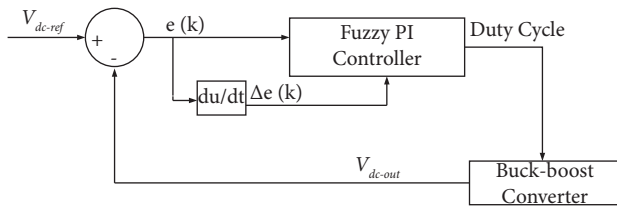
FIGURE 10: Control of the two-level buck-boost converter to the DFIG.

unbalanced loads and the proposed SC-integrated APF are connected to PCC. Also, the DFIGs are connected to the ESS through the two-level buck-boost converter.

5. Results and Discussion

5.1. Application of Nonlinear Unbalanced Loads. First, the nonlinear unbalanced loads are applied to the electric network to deduce the effectiveness of the system to suppress harmonics and compensate for the reactive power. Power systems must consider total harmonic distortion (THD), which must be kept as low as possible. Higher power factor, lower peak currents, and more efficiency result from decreased THD in power systems. The nonlinear load model consists of a bridge rectifier connected to a resistive and inductive load. Two types of loads are studied: low inductive loads and high inductive loads.

5.1.1. Low Inductive Load. First, the SC-integrated APF is applied with a low inductive load connected to PCC. Figure 12(a) illustrates the voltage waveform at B575 that has a THD of 2.84% without the SC-integrated APF. The load current waveform and its FFT analysis are illustrated in Figures 12(b) and 12(c), respectively, which illustrate that the current is highly nonsinusoidal and that the load current's THD equals 44.37%. The reactive power absorbed by the load equals 2.9 kVAR, as shown in Figure 12(d). The impact of adopting the SC-integrated APF is illustrated in Figure 13, which appeared in the load current and absorbed reactive power. The voltage waveform at B575 is shown in Figure 13(a) that illustrates that the THD equals 2.84%. Figures 13(b) and 13(c) illustrate the load current waveform and its FFT analysis, and in this case, the current waveform is improved and becomes more sinusoidal and the THD decreased to 7.8%. With the SC-integrated APF, the load does not absorb reactive power but instead delivers about 4 kVAR, as shown in Figure 13(d).

5.1.2. High Inductive Load. In this case, a high inductive load coupled at the PCC is used in conjunction with an SC-integrated APF application. Figure 14(a) shows the voltage waveform at B575 which has a THD of 4.25% without the SC-integrated APF. Figures 14(b) and 14(c) depict the load current waveform and its FFT analysis, respectively, indicating that the current is highly nonsinusoidal and much distorted and that the load current's THD is 38.68%. According to Figure 14(d), the load's reactive power absorption is 370 kVAR. Figure 15 presents the SC-integrated APF impact, which is manifested in the load voltage, current, and absorbed reactive power. Figure 15(a) displays the voltage waveform at B575 and depicts the THD, which equals 3.92%. The load current waveform and its associated FFT analysis are shown in Figures 15(b) and 15(c), and in this case, the current waveform is improved and becomes less distorted and the THD decreased to 16.67%. The SC-integrated APF enables the load to deliver approximately 145 kVAR rather than absorbing reactive power, as shown in Figure 15(d).

5.2. Application of Different Types of Faults. To deduce the effectiveness of the integration of the SC with the APF, different types of faults such as single-line-to-ground, double-line-to-ground fault, and three-line-to-ground faults are applied to the network. The results with using the SC-integrated APF are compared with that using a simple APF.
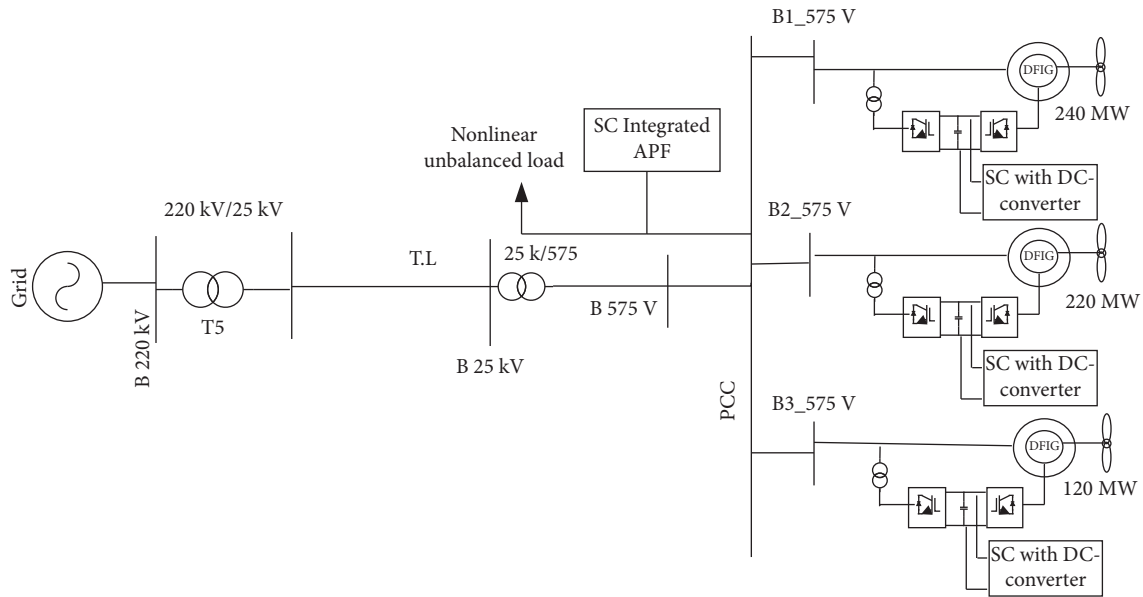
FIGURE 11: Layout of the studied model.

5.2.1. Single-Line-to-Ground Fault. A single-line-to-ground fault is applied at B575 at 1 sec time with a fault duration of 250 msec. The AC voltage at B575 is shown in Figure 16(a) that illustrates that a fault occurred in phase *A* and that the voltage at phases *B* and *C* dropped to 50% of its normal value. The DC voltage of APF capacitor performance is shown in Figure 16(b). Without the SC circuit, the DC voltage dropped to 1180 V during faults and returned to its normal value (1200 V) at 1.6 sec. However, the DC voltage almost remained unchanged during the fault with using the SC circuit. Figure 16(c) shows that the load active power performance is the same whether with employing SC or without. However, utilizing SC had an impact on the load's reactive power since it absorbed 500 VAR during the fault, as shown in Figure 16(d). On the other side, it absorbed 700 VAR without SC, but with or without SC, overshoot equals 1380 VAR. Figure 16(e) illustrates the DC-link voltage of the back-to-back converter capacitor performance. Without SC, the overshoot equals to 1.4 kV, and then, the voltage oscillated between 1.2 kV and 1.4 kV; however, overshoot equals 1.18 kV with SC, and the voltage returned to its steady-state value (1.15 kV). The total active power of the wind farm performance is illustrated in Figure 16(f). The total active power dropped to 200 MW before returning to the steady condition at 1.45 sec with using SC. However, it dropped to 160 MW and reached the steady state without using SC at 1.9 seconds. Utilizing SC has the effect of bringing the total reactive power to the steady state faster than it would without SC, as it reached its steady-state value at 1.45 sec with using SC and at 1.9 sec without using SC, as illustrated in Figure 16(g).

5.2.2. Double-Line-to-Ground Fault. At B575, a double-line-to-ground fault is applied at 1 sec time with 250 msec fault duration. Figure 17(a) depicts the AC voltage at B575, which illustrates that a fault occurred in phase *A* and *B* and that the voltage at phase *C* dropped to less than 50% of its normal value. Figure 17(b) depicts the DC voltage performance of the APF capacitor. Without the SC circuit, the DC voltage decreased to 1163 V during the fault and then recovered to its original level (1200 V) at 1.67 sec. However, when a fault occurred with using the SC circuit, the DC voltage has very low oscillation and nearly stayed unchanged. Figure 17(c) shows that there is no noticeable effect of using SC on the load active power performance. However, as can be seen in Figure 17(d), using SC had an influence on the load's reactive power since it absorbed only 500 VAR with an overshoot of 8 kVAR during the fault. On the other side, it absorbed 2000 VAR without SC with an overshoot of 8.7 kVAR. The DC-link voltage of the back-to-back converter capacitor performance is shown in Figure 17(e). Without SC, overshoot reached 1.95 kV and then reduced to 1.088 kV and returned to its normal value (1.15 kV) at 1.25 sec. However, with SC, the DC-link voltage has very low oscillation between 1.16 and 1.13 kV during fault duration. Figure 17(f) shows that the total active power decreased to 81 MW until stabilizing with SC at 1.45 seconds. However, without SC, it decreased to 52 MW, and after 1.9 seconds, it achieved a stable state. The instant at which the total reactive power has reached its steady-state value is 1.45 sec with SC and 1.9 sec without SC, as illustrated in Figure 17(g).
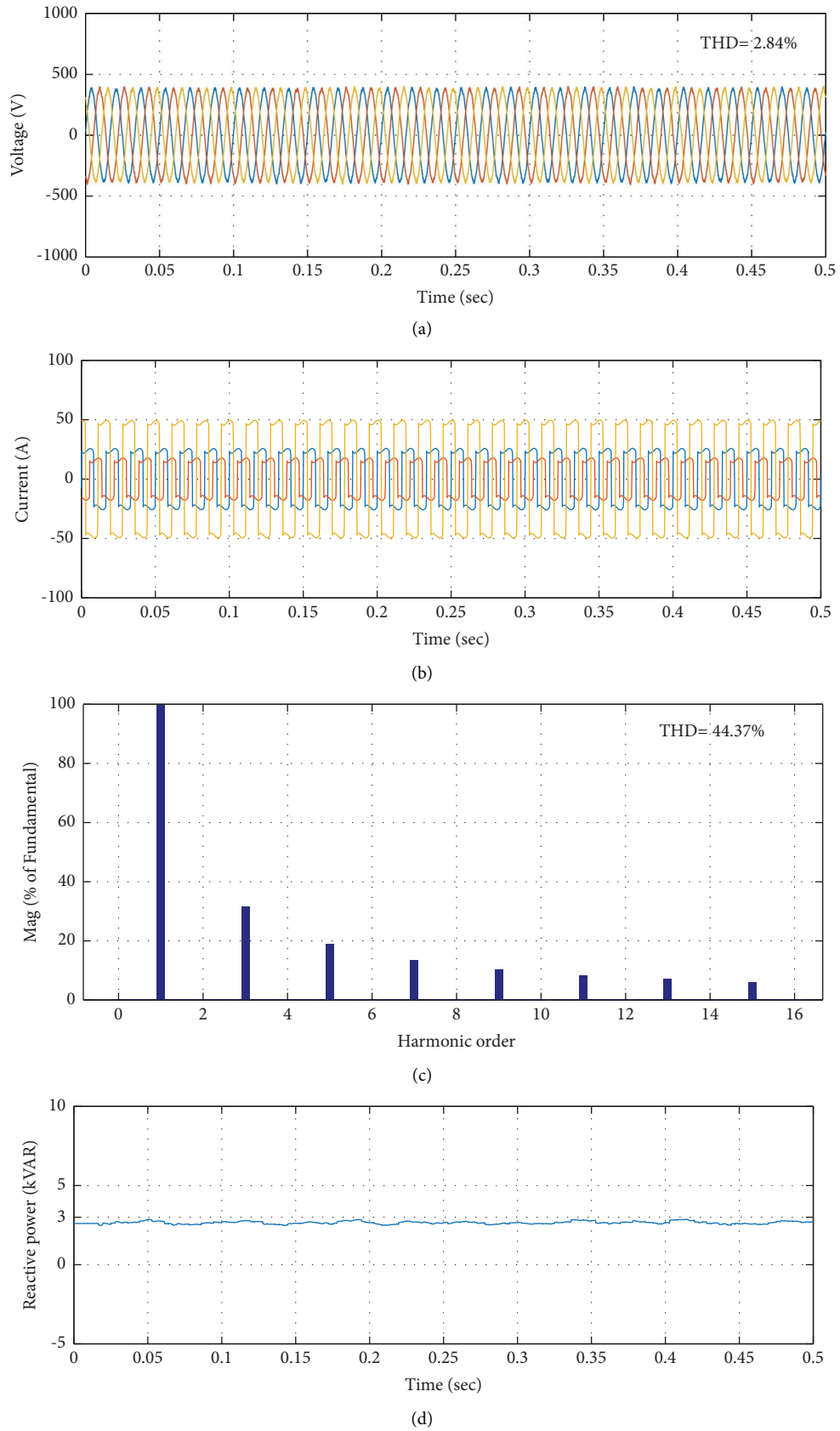
FIGURE 12: Performance during light nonlinear loading without SC-integrated APFs. (a) Load voltage waveform, (b) load current waveform, (c) FFT analysis of load current, and (d) reactive power of the load.
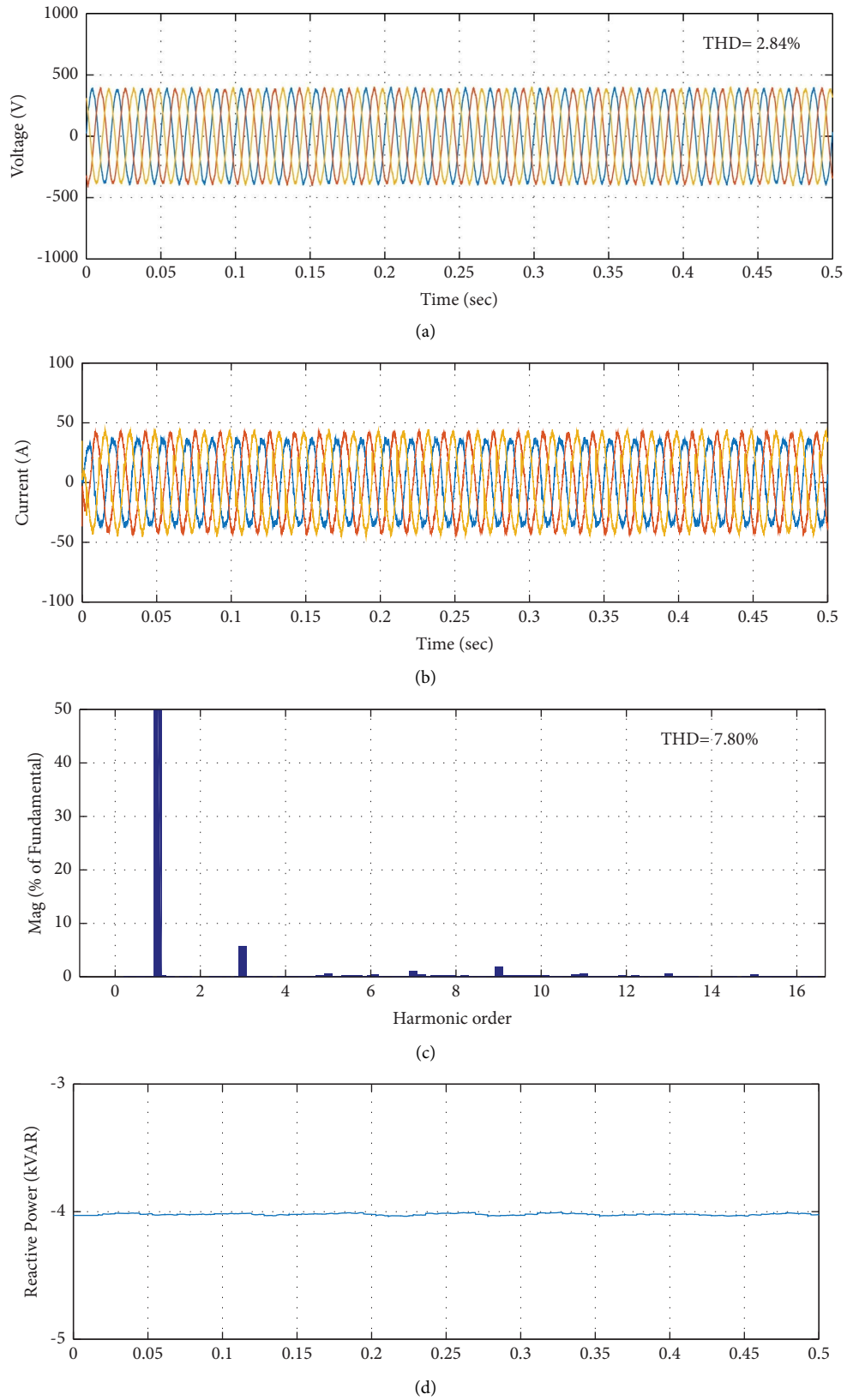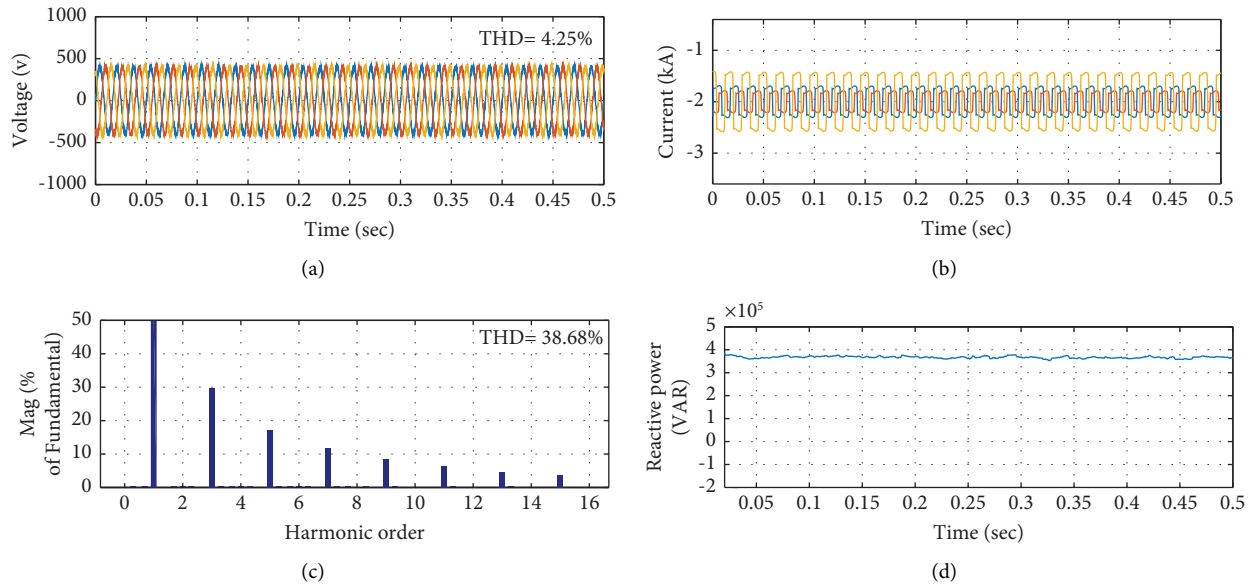
(a)

(b)

(c)

(d)

FIGURE 13: Performance during light nonlinear loading with SC-integrated APFs. (a) Load voltage waveform, (b) load current waveform, (c) FFT analysis of load current, and (d) reactive power of the load.
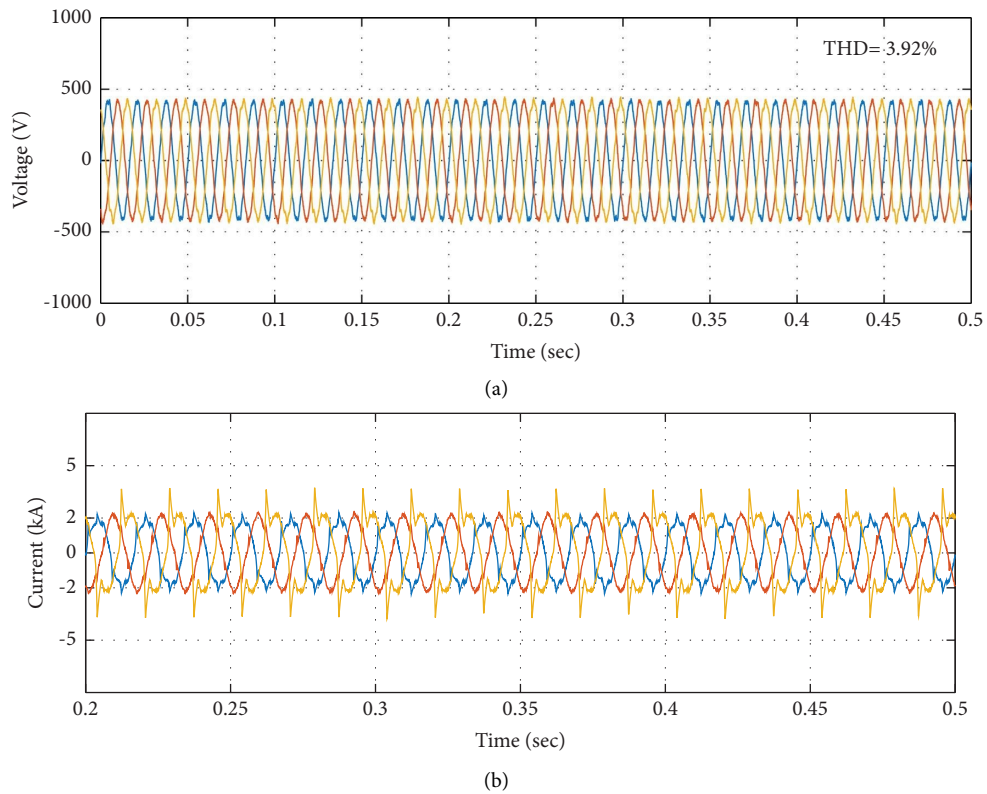
FIGURE 14: Performance during heavy nonlinear loading without SC-integrated APFs. (a) Load voltage waveform, (b) load current waveform, (c) FFT analysis of load current, and (d) reactive power of the load.
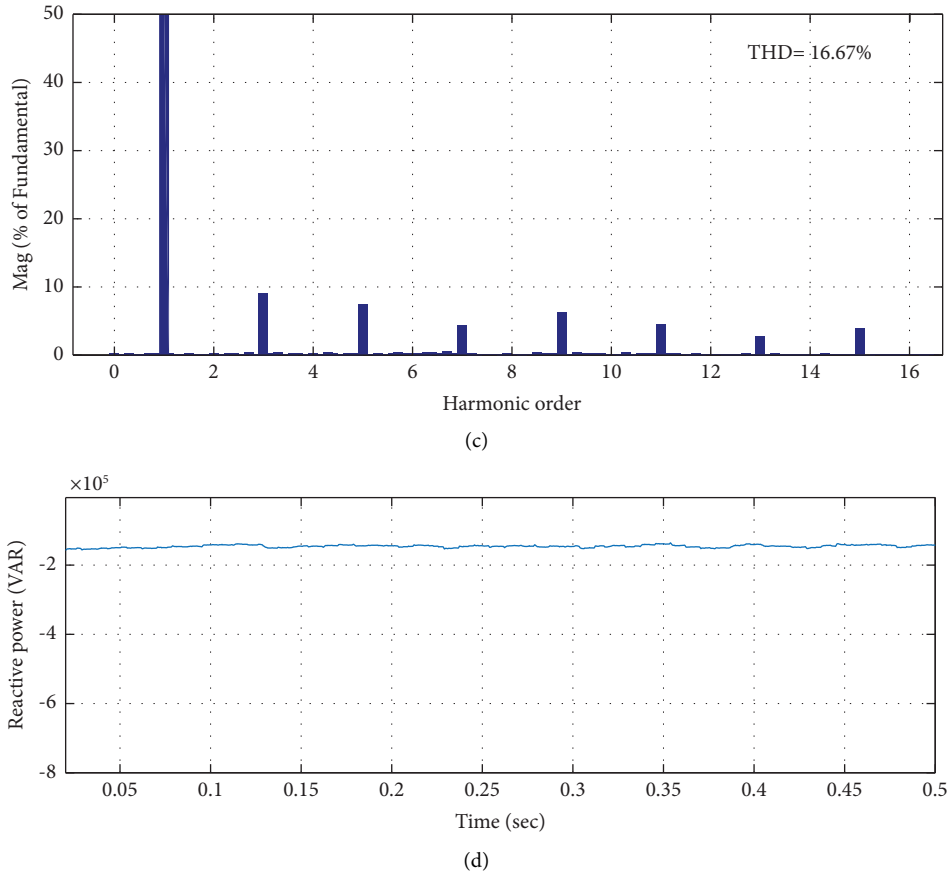

FIGURE 15: Continued.

(c)

(d)

FIGURE 15: Performance during heavy nonlinear loading with SC-integrated APFs (a) Load voltage waveform, (b) load current waveform, (c) FFT analysis of load current, and (d) reactive power of the load.
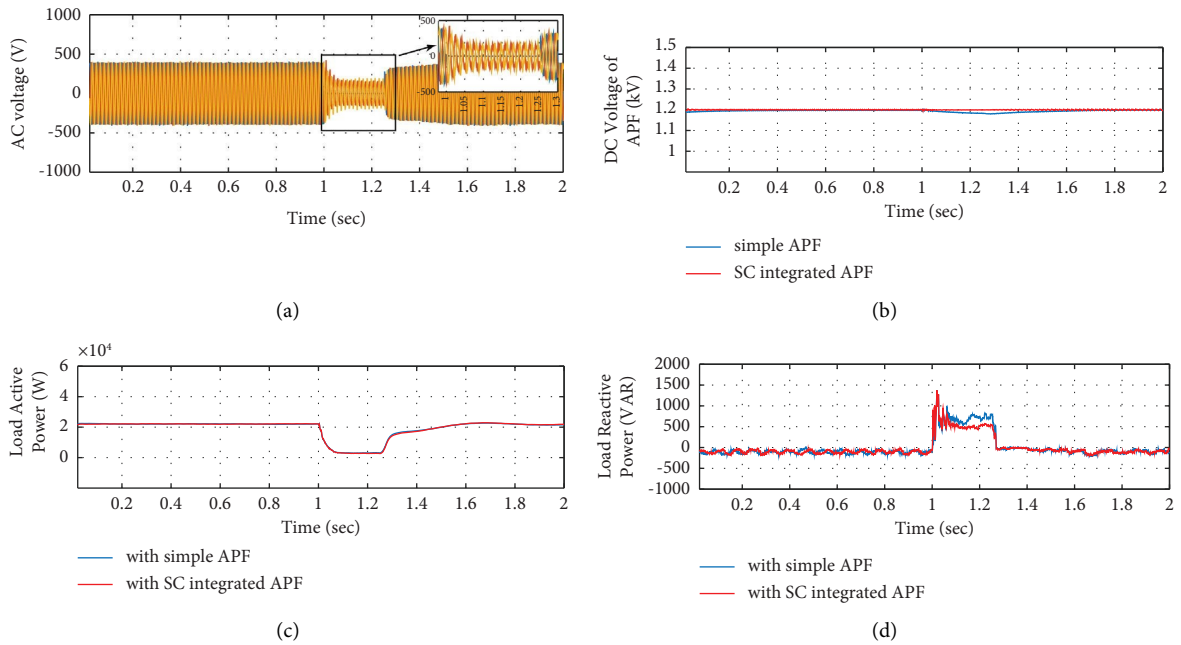

(a)

(b)
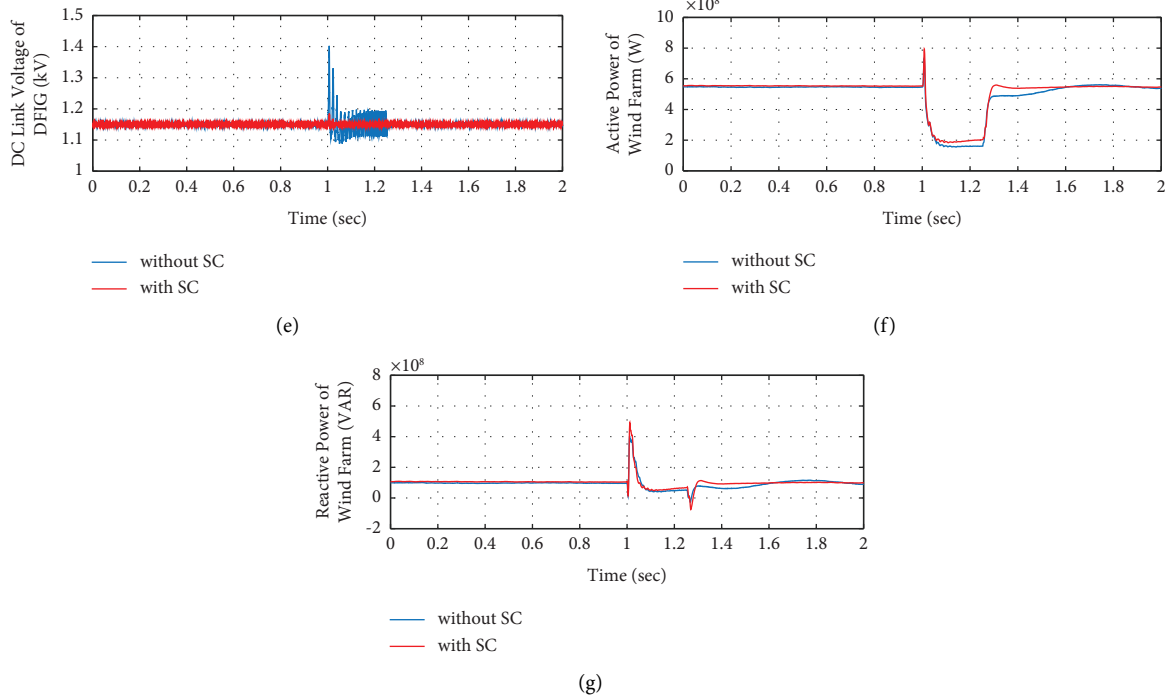

(c)

(d)

FIGURE 16: Continued.

(e)

(f)

(g)

FIGURE 16: Performance during a single-line-to-ground fault. (a) The AC voltage at B575, (b) the DC voltage of the APF capacitor, (c) the load active power, (d) the load reactive power, (e) the DC-link voltage of the back-to-back converter, (f) the total active power of the wind farm, and (g) the total reactive power of the wind farm.

(a)

(b)

(c)

(d)

FIGURE 17: Continued.

(e)

(f)

(g)

FIGURE 17: Performance during a double-line-to-ground fault. (a) The AC voltage at B575, (b) the DC voltage of the APF capacitor, (c) the load active power, (d) the load reactive power, (e) the DC-link voltage of the back-to-back converter, (f) the total active power of the wind farm, and (g) the total reactive power of the wind farm.
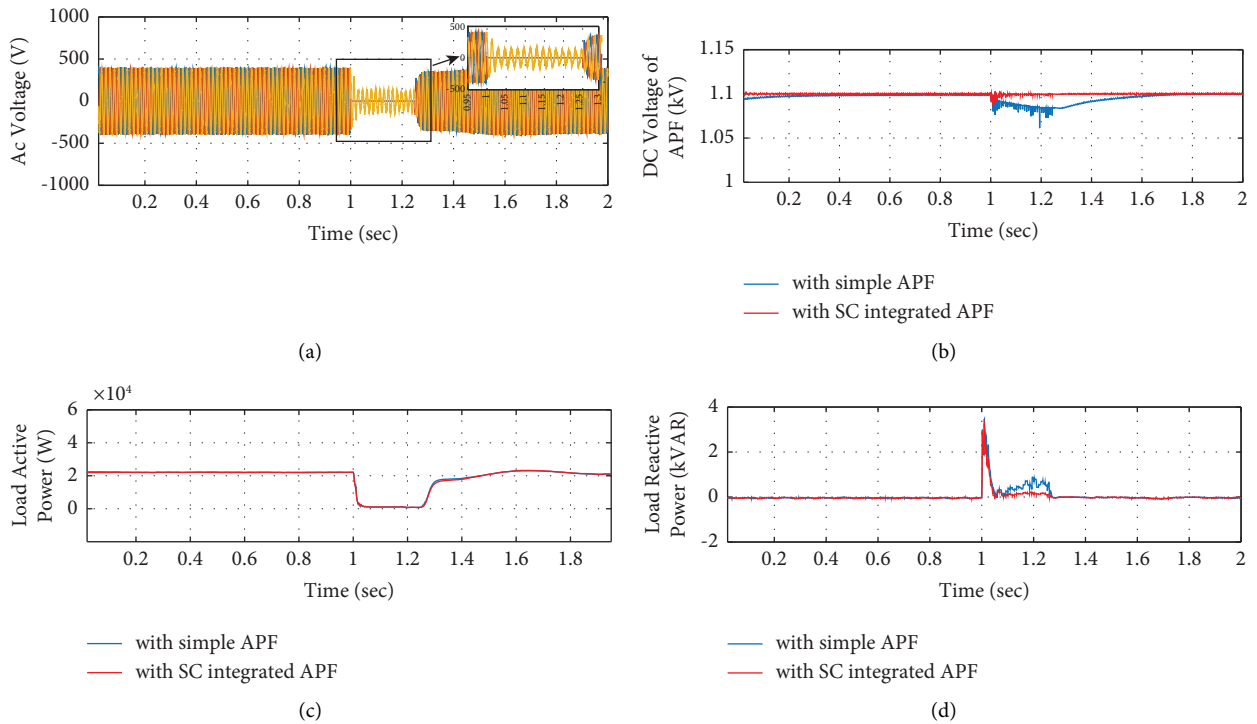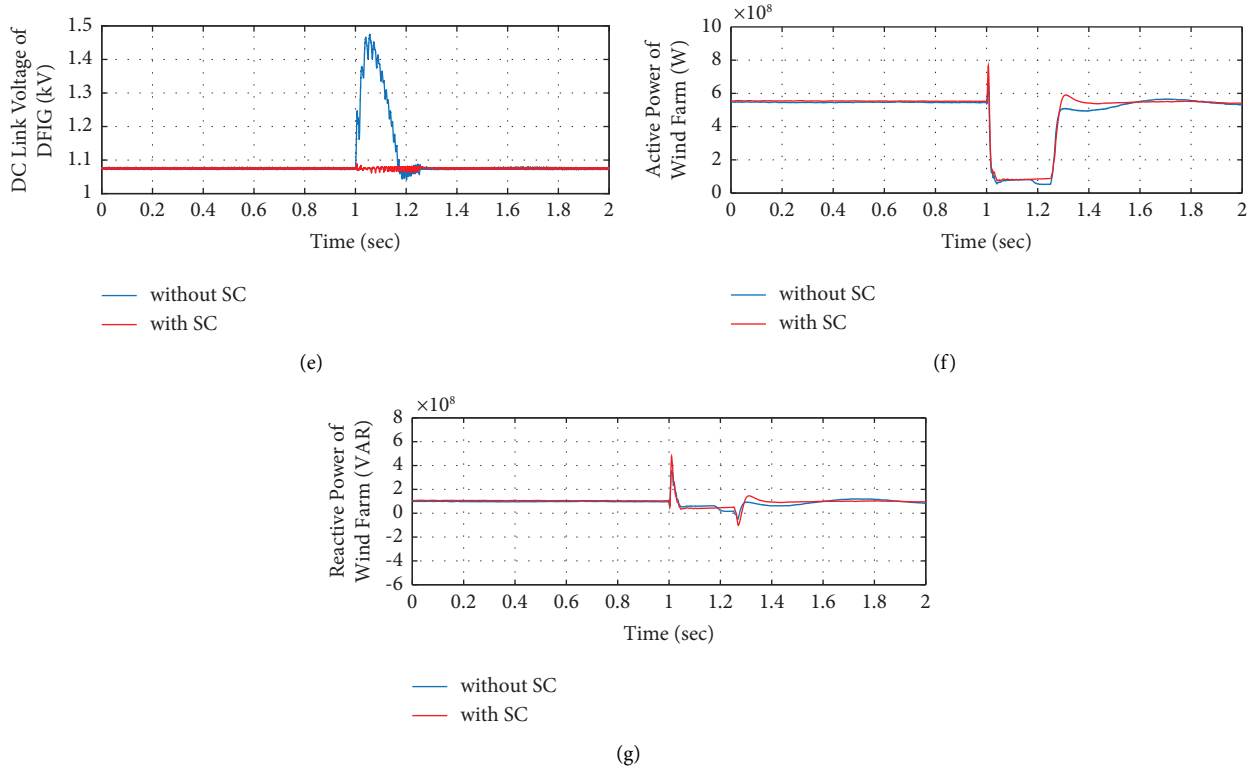

(a)

(b)

(c)

(d)

FIGURE 18: Continued.

(e)

(f)

(g)

FIGURE 18: Performance during a three-line-to-ground fault. (a) The AC voltage at B575, (b) the DC voltage of the APF capacitor, (c) the load active power, (d) the load reactive power, (e) the DC-link voltage of the back-to-back converter, (f) the total active power of the wind farm, and (g) the total reactive power of the wind farm.
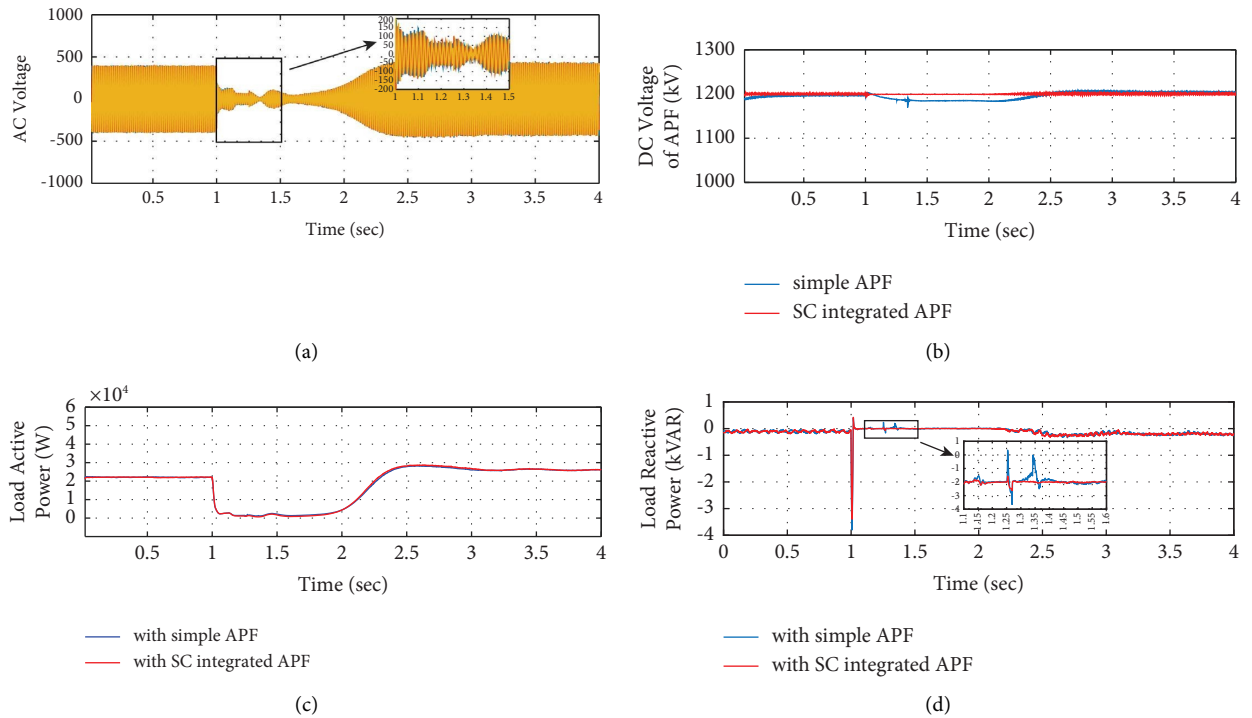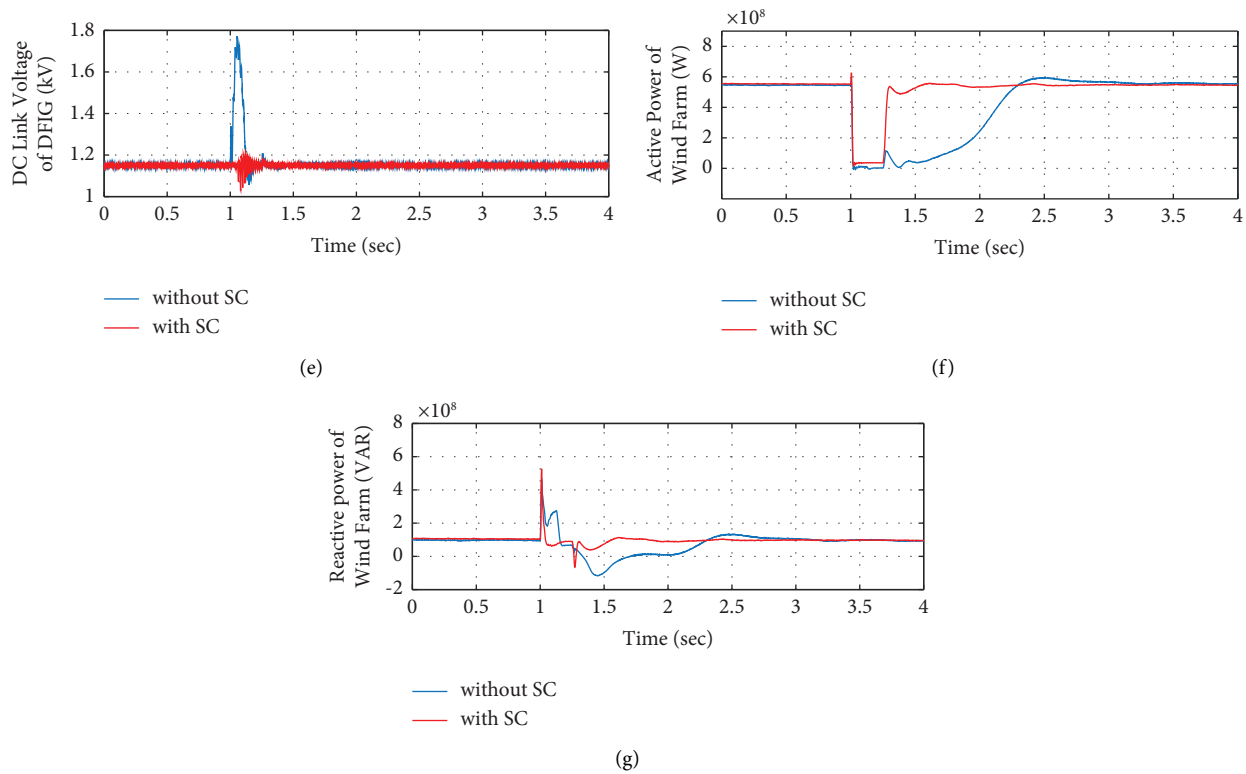
5.2.3. Three-Line-to-Ground Fault. A three-line-to-ground fault with a 250 msec fault period is applied at B25 at 1 sec. Figure 18(a) indicates the AC voltage at B575 that illustrates how much the voltage sag occurred in the three phases. Figure 18(b) illustrates the performance of the DC voltage of the APF capacitor. During the fault, the DC voltage reduced to 1185 V without using SC and then returned to 1200 V (which is the normal value) at 3.12 sec. However, because of the SC circuit effect, the DC voltage essentially stayed unaltered. As in the previous cases (single and double-line faults), the active power has no effect with using SC, as shown in Figure 18(c); however, the impact of SC appears on reactive power performance, as illustrated in Figure 18(d). With SC, the overshoot of reactive power is −3350 VAR and then has a zero VAR value during the fault; however, the overshoot of reactive power is −3800 VAR without SC, and then, it has oscillated between 230 VAR and −164 VAR. The DC-link voltage of the back-to-back converter capacitor performance is illustrated in Figure 18(e). Without SC, overshoot equals 1771 V during the fault and then returned to its normal value (1150 V) at 1.57 sec; however, it has very little oscillation between 1200 V and 1029 V with SC and then recovered its normal value at 1.3 sec. The total active power of the wind farm dropped to 36 MW during the fault and returned to the steady condition at 2.5 sec with using the SC circuit, as shown in Figure 18(f). Without SC, the active power dropped to 2 MW and returned to the steady condition at 3.2 sec. Figure 18(g) shows that the total reactive power has reached its steady value at 2 sec with SC and 3 sec without SC.

6. Conclusions

The integration of SC with the three-phase four-wire APF is suggested in this study utilizing an interfaced three-level bidirectional buck-boost converter that is fuzzy control-assisted. The basic objectives of the SC-integrated APF are to regulate the DC voltage of the APF's DC link and absorb fluctuations in the compensated reactive power during disturbances. A wind farm of Gabal El-Zeit with a capacity of 580 MW that is connected to unbalanced nonlinear loads serves as the study model. First, a low inductive load connected to PCC is applied. Without the SC-integrated APF, the load current's THD equals 44.37%, the load voltage's THD equals 2.84%, and the reactive power absorbed by the load equals 2.9 kVAR. With the SC-integrated APF, the current's THD equals 7.8%, the load voltage's THD equals 2.84%, and the load does not absorb reactive power but instead delivers about 4 kVAR. Then, a high inductive load is applied at PCC. Without the SC-integrated APF, the load current's THD is 38.68%, the load voltage's THD equals 4.25%, and the load's reactive power absorption is 370 kVAR. With the SC-integrated APF, the load current's THD is 16.67%, the load voltage's THD equals 3.92%, and the load does not absorb reactive power but instead delivers about 4 kVAR. For deducing the

effectively of SC integration, a single-line-to-ground fault is applied at PCC at 1 sec for 250 msec. Without the SC circuit, the DC voltage dropped to 1180 V during the fault and returned to its normal value (1200 V) at 1.6 sec and the load absorbed 700 VAR during the fault. With the SC circuit, the DC voltage of the APF almost remained unchanged and the load absorbed 500 VAR during the fault. The load active power performance is the same whether with employing SC or without. Without SC, the DC-link voltage of the back-to-back converter capacitor has overshot to 1.4 kV and then oscillated between 1.2 kV and 1.4 kV; however, overshoot has got to 1.18 kV with SC and returned to its steady-state value (1.15 kV). The total active power of the wind farm dropped to 200 MW before returning to the steady condition at 1.45 sec with SC. However, it dropped to 160 MW and reached the steady state without SC at 1.9 seconds. Then, a double-line-to-ground fault is applied at PCC at 1 sec for 250 msec. Without an SC circuit, the DC voltage of the APF decreased to 1163 V and then recovered to its original level at 1.67 sec and the load absorbed 2000 VAR with 8.7 kVAR overshoot. With the SC circuit, the DC voltage has very low oscillation and nearly stayed unchanged and the load absorbed only 500 VAR with 8 kVAR overshoot during the fault. The total active power of the wind farm decreased to 81 MW until stabilizing with SC at 1.45 seconds. However, without SC, it decreased to 52 MW, and after 1.9 seconds, it achieved a stable state. The time when the total reactive power has reached its steady value is at 1.45 sec with SC and 1.9 sec without SC. A three-line-to-ground fault is applied at B25 at 1 sec for 250 msec. Without SC, the DC voltage reduced to 1185 V and then returned to 1200 V at 3.12 sec and the overshoot of reactive power is −3800 VAR, and it has oscillated between 230 VAR and −164 VAR. With SC, the DC voltage essentially stayed unaltered and the overshoot of reactive power is −3350 VAR and then has a zero VAR value during the fault. The total active power of the wind farm dropped to 36 MW during the fault and returned to the steady condition at 2.5 sec with using the SC circuit. Without SC, the active power dropped to 2 MW and returned to the steady condition at 3.2 sec. The total reactive power has reached its steady value at 2 sec with SC and 3 sec without SC. The results indicate a satisfactory performance of the proposed methodology to increase the system's stability.

Abbreviations

APF: Active power filter
VSI: Voltage source inverter
ESS: Energy storage system
SC: Supercapacitor
FLC: Fuzzy logic control
PCC: Point of common coupling
DFIG: Doubly fed induction generator
GSC: Grid-side converter
RSC: Rotor-side converter
FACTS: Flexible alternating current transmission system
THD: Total harmonic distortion.

Data Availability

The data used to support the findings of this study are included within the article.

Conflicts of Interest

The authors declare that they have no conflicts of interest.

References

[1] A. K. Dubey, J. P. Mishra, and A. Kumar, "Comparative analysis of ROGI based shunt active power filter under current fed and voltage fed type non-linear loading condition," *IFAC-PapersOnLine*, vol. 55, no. 1, pp. 156–161, 2022.
[2] A. K. Mishra, S. R. Das, P. K. Ray, R. K. Mallick, A. Mohanty, and D. K. Mishra, "PSO-GWO optimized fractional order PID based hybrid shunt active power filter for power quality improvements," *IEEE Access*, vol. 8, pp. 74497–74512, 2020.
[3] T. Toumi, A. Allali, A. Meftouhi, O. Abdelkhalek, A. Benabdelkader, and M. Denai, "Robust control of series active power filters for power quality enhancement in distribution grids: simulation and experimental validation," *ISA Transactions*, vol. 107, pp. 350–359, 2020.
[4] G. D. S. Fischer, A. Mengatto, L. G. Kremer, and M. Mezaroba, "A control strategy for a series APF with critical-load-bus voltage feedback that avoids injection transformer saturation," *IEEE Transactions on Industry Applications*, vol. 55, no. 3, pp. 2290–2299, 2019.
[5] L. Wang, C.-S. Lam, and M.-C. Wong, "Hybrid structure of static var compensator and hybrid active power filter (SVC//HAPF) for medium-voltage heavy loads compensation," *IEEE Transactions on Industrial Electronics*, vol. 65, no. 6, pp. 4432–4442, 2018.
[6] Y. Han, L. Xu, M. M. Khan, C. Chen, G. Yao, and L.-D. Zhou, "Robust deadbeat control scheme for a hybrid APF with resetting filter and ADALINE-based harmonic estimation algorithm," *IEEE Transactions on Industrial Electronics*, vol. 58, pp. 3893–3904, 2010.
[7] L. R. Limongi, L. R. da Silva Filho, L. G. B. Genu, F. Bradaschia, and M. C. Cavalcanti, "Transformerless hybrid power filter based on a six-switch two-leg inverter for improved harmonic compensation performance," *IEEE Transactions on Industrial Electronics*, vol. 62, no. 1, pp. 40–51, 2015.
[8] S. Echalih, A. Abouloifa, J. Janik et al., "Hybrid controller with fuzzy logic technique for three phase half bridge interleaved buck shunt active power filter," *IFAC-PapersOnLine*, vol. 53, no. 2, pp. 13418–13423, 2020.
[9] J. Fei, H. Wang, and M. Hua, "Double-hidden-layer recurrent neural network fractional-order sliding mode control of shunt active power filter," *IFAC-PapersOnLine*, vol. 53, no. 2, pp. 6232–6237, 2020.
[10] S. Khalid, "Performance evaluation of Adaptive Tabu search and Genetic Algorithm optimized shunt active power filter using neural network control for aircraft power utility of 400 Hz," *Journal of Electrical Systems and Information Technology*, vol. 5, no. 3, pp. 723–734, 2018.
[11] R. Chilipi, N. Al Sayari, and J. Y. Alsawalhi, "Control of single-phase solar power generation system with universal active power filter capabilities using least mean mixed-norm (LMMN)-based adaptive filtering method," *IEEE Transactions on Sustainable Energy*, vol. 11, no. 2, pp. 879–893, 2020.
[12] G. Son, H.-J. Kim, and B.-H. Cho, "Improved modulated carrier control with on-time doubler for a single-phase shunt

active power filter," *IEEE Transactions on Power Electronics*, vol. 33, no. 2, pp. 1715–1723, 2018.

[13] M. Pichan, M. Seyyedhosseini, and H. Hafezi, "A new DeadBeat-based direct power control of shunt active power filter with digital implementation delay compensation," *IEEE Access*, vol. 10, pp. 72866–72878, 2022.

[14] B. N. Rao, Y. Suresh, A. K. Panda, B. S. Naik, and V. Jammala, "Development of cascaded multilevel inverter based active power filter with reduced transformers," *CPSS Transactions on Power Electronics and Applications*, vol. 5, no. 2, pp. 147–157, 2020.

[15] W. U. K. Tareen and S. Mekhielf, "Three-phase transformerless shunt active power filter with reduced switch count for harmonic compensation in grid-connected applications," *IEEE Transactions on Power Electronics*, vol. 33, no. 6, pp. 4868–4881, 2018.

[16] X. Nie and J. Liu, "Current reference control for shunt active power filters under unbalanced and distorted supply voltage conditions," *IEEE Access*, vol. 7, pp. 177048–177055, 2019.

[17] B. Rouabah, H. Toubakh, and M. Sayed-Mouchaweh, "Fault tolerant control of multicellular converter used in shunt active power filter," *Electric Power Systems Research*, vol. 188, pp. 106533–106621, 2020.

[18] Y. Bekakra, L. Zellouma, and O. Malik, "Improved predictive direct power control of shunt active power filter using GWO and ALO–Simulation and experimental study," *Ain Shams Engineering Journal*, vol. 12, no. 4, pp. 3859–3877, 2021.

[19] S. S. Patnaik and A. K. Panda, "Three-level H-bridge and three H-bridges-based three-phase four-wire shunt active power filter topologies for high voltage applications," *International Journal of Electrical Power & Energy Systems*, vol. 51, pp. 298–306, 2013.

[20] X. Sun, R. Han, H. Shen, B. Wang, Z. Lu, and Z. Chen, "A double-resistive active power filter system to attenuate harmonic voltages of a radial power distribution feeder," *IEEE Transactions on Power Electronics*, vol. 31, no. 9, pp. 6203–6216, 2016.

[21] T. Gao, Y. Lin, D. Chen, and L. Xiao, "A novel active damping control based on grid-side current feedback for LCL-filter active power filter," *Energy Reports*, vol. 6, pp. 1318–1324, 2020.

[22] J. Fang, G. Xiao, X. Yang, and Y. Tang, "Parameter design of a novel series-parallel-resonant LCL filter for single-phase half-bridge active power filters," *IEEE Transactions on Power Electronics*, vol. 32, no. 1, pp. 200–217, 2017.

[23] L. Wang, C.-S. Lam, and M.-C. Wong, "Unbalanced control strategy for a thyristor-controlled LC-coupling hybrid active power filter in three-phase three-wire systems," *IEEE Transactions on Power Electronics*, vol. 32, no. 2, pp. 1056–1069, 2017.

[24] D. Chen, L. Xiao, W. Yan, Y. Li, and Y. Guo, "A harmonics detection method based on triangle orthogonal principle for shunt active power filter," *Energy Reports*, vol. 7, pp. 98–104, 2021.

[25] D. Chen, L. Xiao, H. Lian, and Z. Xu, "A fault tolerance method based on switch redundancy for shunt active power filter," *Energy Reports*, vol. 7, pp. 449–457, 2021.

[26] L. Morán, J. Dixon, and M. Torres, "Active power filters," in *Power Electronics Handbook*, pp. 1341–1379, Elsevier, Amsterdam, Netherlands, 2018.

[27] W.-H. Choi, C.-S. Lam, M.-C. Wong, and Y.-D. Han, "Analysis of dc-link voltage controls in three-phase four-wire hybrid active power filters," *IEEE Transactions on Power Electronics*, vol. 28, no. 5, pp. 2180–2191, 2013.

[28] New and Renewable Energy Authority, "Renewable energy indication," 2022, http://www.nrea.gov.eg/.

[29] I. Hamdan, M. M. M. Youssef, and O. Noureldeen, "Design of fuzzy coordinated PI controller for supercapacitor in large scale wind farm," in *Proceedings of the 2021 22nd International Middle East Power Systems Conference (MEPCON)*, pp. 416–423, Assiut, Egypt, December 2021.

[30] S. AlGhamdi, I. Hamdan, M. M. M. Youssef, and O. Noureldeen, "Development and application of fuzzy proportional-integral control scheme in pitch angle compensation loop for wind turbines," *Machines*, vol. 9, no. 7, p. 135, 2021.